



Smart bandage with integrated multifunctional sensors based on MXene-functionalized porous graphene scaffold for chronic wound care management

Md. Sharifuzzaman, Ashok Chhetry, Md Abu Zahed, Sang Hyuk Yoon, Chan I. Park,
Shipeng Zhang, Sharat Chandra Barman, Sudeep Sharma, Hyosang Yoon, Jae Yeong Park *

Department of Electronic Engineering, Advanced Sensor and Energy Research (ASER) Laboratory, Kwangwoon University, 447-1, Seoul, 139-701, Republic of Korea



ARTICLE INFO

Keywords:
2D MXene functionalized 3D LGG sheets
C–O–Ti covalent crosslink
LGG-MXene hybrid scaffold
Smart bandage
Integrated multifunctional sensors

ABSTRACT

Three-dimensional (3D) porous laser-guided graphene (LGG) electrodes on elastomeric substrates are of great significance for developing flexible functional electronics. However, the high sheet resistance and poor mechanical properties of LGG sheets obstruct their full exploitation as electrode materials. Herein, we applied 2D MXene nanosheets to functionalize 3D LGG sheets via a C–O–Ti covalent crosslink to obtain an LGG-MXene hybrid scaffold exhibited high conductivity and improved electrochemistry with fast heterogeneous electron transfer (HET) rate due to the synergistic effect between LGG and MXene. Then we transferred the obtained hybrid scaffold onto PDMS to engineer a smart, flexible, and stretchable multifunctional sensors-integrated wound bandage capable of assessing uric acid (UA), pH, and temperature at the wound site. The integrated UA sensor exhibited a rapid response toward UA in an extended wide range of 50–1200 μM with a high sensitivity of 422.5 μA mM⁻¹ cm⁻² and an ultralow detection limit of 50 μM. Additionally, the pH sensor demonstrated a linear Nernstian response ($R^2 = 0.998$) with a high sensitivity of $-57.03 \text{ mV pH}^{-1}$ in the wound relevant pH range of 4–9. The temperature sensor exhibited a fast and stable linear resistive response to the temperature variations in the physiological range of 25–50 °C with an excellent sensitivity and correlation coefficient of 0.09% °C⁻¹ and 0.999, respectively. We anticipate that this stretchable and flexible smart bandage could revolutionize wound care management and have profound impacts on the therapeutic outcomes.

1. Introduction

In recent years, the emergence of stretchable and flexible electronics for wearable biomedical applications has garnered significant attention, which demands unconventional fabrication and patterning strategies for proper transducing materials onto flexible substrates (for example, ecoflex, PDMS, and polyurethane). Several groups have addressed these issues by designing stretchable and flexible electrodes with good performance and conductivity using diverse active materials, such as graphene (Hui et al., 2019), carbon nanotubes (CNT) (Kobylko et al., 2014), conductive polymers (Zahed et al., 2020), silver nanowires (AgNWs) (Xuan et al., 2018), hybrid materials (Nguyen et al., 2012), and copper nanowires (CuNWs) (Zhang et al., 2019). Among these, carbon-based scaffolds have drawn significant attention owing to their unique inherent properties, such as the large active surface area, high electron mobility, stability, and easy functionalization (Park et al., 2013; Rahimi

et al., 2016).

Laser-guided graphene (LGG), a two-dimensional (2D) porous graphitic nanomaterial with the desired terminal groups, produced through a computer-controlled one-step laser writing process of polyimide (PI) film under optimized conditions, has been broadly investigated as a promising electrode material for flexible sensors, supercapacitors, electrocatalysts, and environmental applications (Barman et al., 2020; Song et al., 2018; Sun et al., 2018; Tittle et al., 2018; Zahed et al., 2020). It offers a hierarchical porous three-dimensional (3D) interconnected multilayer graphene network that is suitable for wearable applications. However, LGG sheets suffer from high sheet resistance, low electrical performance, and poor mechanical properties when transferred onto stretchable and flexible substrates such as ecoflex, PDMS, and polyurethane. A major challenge is to engineer strategies simultaneously to enhance the electrical performance and mechanical properties of LGG sheets for stretchable and

* Corresponding author.

E-mail address: jaepark@kw.ac.kr (J.Y. Park).

flexible applications. These challenges can be potentially solved by introducing 2D active nanosheets and nanomaterials (e.g., GO, rGO, MoS₂, and CNT) onto 3D microporous structures through different interfacial interactions, such as ionic bonding, covalent bonding, hydrogen bonding, and π - π bridging (Ma et al., 2018; Zhou et al., 2020).

Recently, a novel class of 2D multilayered nanosheets (MXenes) with enhanced metallic conductivity, large surface area, high stability, high strength, and inherent electrochemical properties has demonstrated significant potential for applications in supercapacitors (Ghidiu et al., 2014; Jiang et al., 2018), sensors (L. Liu et al., 2019; J. Liu et al., 2019; Wu et al., 2018), electronics (Kim et al., 2019), and catalysis (Seh et al., 2016; Zhao et al., 2017). Ti₃C₂T_x, the most promising of the 30 synthesized MXenes, is commonly prepared by carefully etching the aluminum (Al) layers from the ternary MAX precursors (Ti₃AlC₂) (Alhabeb et al., 2017). Various surface functional groups (T_x), such as hydroxyl (-OH), oxygen (-O), and fluorine (-F), appeared instead of the Al layers during the etching process (Hope et al., 2016). These oxygen-containing surface functional groups could potentially functionalize 3D LGG sheets. It is possible that the MXene nanosheets react with the carboxyl (-COOH) and hydroxyl groups (-OH) of the LGG sheets at room temperature to form a C-O-Ti covalently cross-linked LGG-MXene hybrid scaffold. Covalent crosslinking in C-O-Ti is essential for obtaining the hybrid scaffold, thereby boosting the binding process of MXene and LGG. The hybrid scaffold fully utilizes the synergistic effect of the large active area of LGG along with the excellent conductivity of MXene, exhibiting good conductivity when transferred onto flexible substrates. Moreover, the 3D-2D (LGG-MXene) hybrid scaffold offers abundant surface functionalities suitable for sensing different biological signals (Gu et al., 2019; Huang et al., 2019). Thus far, to the best of our knowledge, there have been no scientific reports regarding a 3D-2D hybrid scaffold as the electrode material on a transparent stretchable and flexible substrate (PDMS) for wearable biomedical applications.

Chronic wounds (CWs), which generally fail to regenerate the damaged tissue within 3 months, are major healthcare complications that impose a serious burden on the healthcare systems in terms of both the affected patients and financial expenses (Posnett, 2008; Sen et al., 2009). To reduce the burden of CWs on patients and the national healthcare budgets, it is necessary to develop advanced and smart wound diagnosis systems for the continuous assessment of the wound status. Based on the characteristics of specific wounds, such as clean or infected, deep or shallow, and dry or exudative, many wound care dressings have been engineered for the common treatment of CWs (Dabiri et al., 2016). These recent wound care dressings are associated with diverse limitations. The majority of the recent wound dressings are passive and cannot provide real-time information on the wound status and its healing progress (Derakhshandeh et al., 2018). Patients require frequent hospital visits to be continuously assessed by the medical personnel for signs of healing and infection; these frequent visits add extra cost and increase the stress on the patients as well as the medical sector. Therefore, smart bandages with an integrated multifunctional flexible sensor capable of diagnosing the wound status without the need of frequent dressing replacements and hospital visits are highly beneficial. Although researchers have proposed various smart bandages for monitoring the various chemical and physical parameters essential for the wound healing status, most of these have intractable shortcomings; such as the requirement of expensive and cumbersome equipment, presence of medical professionals, lack of flexibility in wearing, uncomfortable dressings, and being non-multifunctional (Pal et al., 2018; Phair et al., 2014; Schremel et al., 2014). Therefore, the fabrication of a facile, low-cost, and flexible smart bandage with integrated multifunctional sensors for accurately detecting various wound parameters could revolutionize wound care management and have profound impacts on the therapeutic outcomes.

Among the various generic physicochemical wound status markers, uric acid (UA), pH, and temperature are considered to play the most

important role in the wound healing process (Pal et al., 2018; Pang et al., 2020). Generally, the UA concentration range in wound biofluid and exudate varies between 220 and 750 μ M, which is mostly related to the colonization of *S. aureus* or *P. aeruginosa* bacteria and normally decreases owing to the catalysis caused by microbial uricase during bacterial infection (Kassal et al., 2015; Sharp and Davis, 2008). Therefore, the continuous measurement of UA in wound exudate is considered to be one of the most specific indicators of wound infection and its status. In addition, the pH value of the wound site has been recognized as an important indicator that provides valuable information about the wound status throughout the healing process (Dargaville et al., 2013). Generally, intact skin and healing wounds demonstrate a slightly acidic state (pH 4–6), whereas infected and nonhealing wounds exhibit more alkaline levels (pH 7–9) (Percival et al., 2014). Furthermore, abnormal temperatures at the wound site are closely related to a high risk of infection, inflammation, and chronicity. Temperatures lower than 33 °C reduce the activities of fibroblasts, neutrophils, and epithelial cells, thereby causing a delay in the wound healing process; however, slightly higher temperatures in the range of 36–38 °C imply a reduction in infection (Salvo et al., 2017). Severe hypothermia has also been associated with acute wound infection (Kurz et al., 1996).

In this study, for the first time, we utilized 2D MXene nanosheets to functionalize 3D porous LGG sheets via C-O-Ti covalent crosslinks to obtain LGG-MXene hybrid scaffolds. Then, we successfully transferred the LGG-MXene hybrid scaffold onto PDMS to engineer a high-performance smart stretchable and flexible multifunctional sensors-integrated wound bandage capable of detecting the UA, pH, and temperature at the wound site. The hybrid scaffold transferred onto PDMS still exhibited high conductivity and improved electrochemistry with a fast heterogeneous electron transfer (HET) rate due to the synergistic effect between LGG and MXene. Most of the existing smart wound dressings capable of monitoring single biomarkers provide limited information about the wound healing status. Therefore, this newly developed smart bandage with integrated multifunctional sensors that can monitor various wound parameters could provide invaluable and exact information about the wound status, and help with the selection of suitable treatment policies. The morphology and physicochemical properties of the produced material and sensors were thoroughly characterized by field emission scanning electron microscopy (FESEM), energy dispersive spectrometry (EDS), X-ray photoelectron spectroscopy (XPS), Raman spectroscopy, X-ray diffraction (XRD), cyclic voltammetry (CV), and electrochemical impedance spectroscopy (EIS).

2. Material and methods

2.1. Instruments and chemicals

The instruments, chemicals, and the preparation of the artificial wound exudate are explained in Supplementary Information (SI) in detail.

2.2. Preparation of exfoliated MXene nanosheets

MXene was prepared according to an optimized method, i.e., minimally intensive layer delamination (Alhabeb et al., 2017). The synthesis procedure and the physical characterizations of the as-prepared MXene nanosheets were described briefly in SI (see Figs. S1 and S2).

2.3. Fabrication of stretchable and flexible smart bandage with integrated sensors

A flexible smart bandage was fabricated with multifunctional sensors including a (i) UA sensor, (ii) pH sensor, and (iii) temperature sensor to accurately monitor chronic wound conditions. The step-by-step fabrication scheme of the proposed stretchable and flexible smart bandage with integrated multifunctional sensors for detecting various

physiochemical wound markers is illustrated in Fig. 1. First, a computer-controlled direct CO₂ laser scribing process (Universal Laser System Company, optimized parameters: power: 17 W, speed: 6 cms⁻¹, and line gap: 0.05 mm (Zahed et al., 2020)) was used to pattern the 3D porous

LGG-enabled multifunctional sensors on commercial PI films (thickness: 50 μm) (Fig. 1A). Subsequently, the exfoliated MXene solution in ethanol with different concentrations (1, 3, and 5 mg mL⁻¹) was carefully pipetted onto the entire LGG sensor pattern to perform the

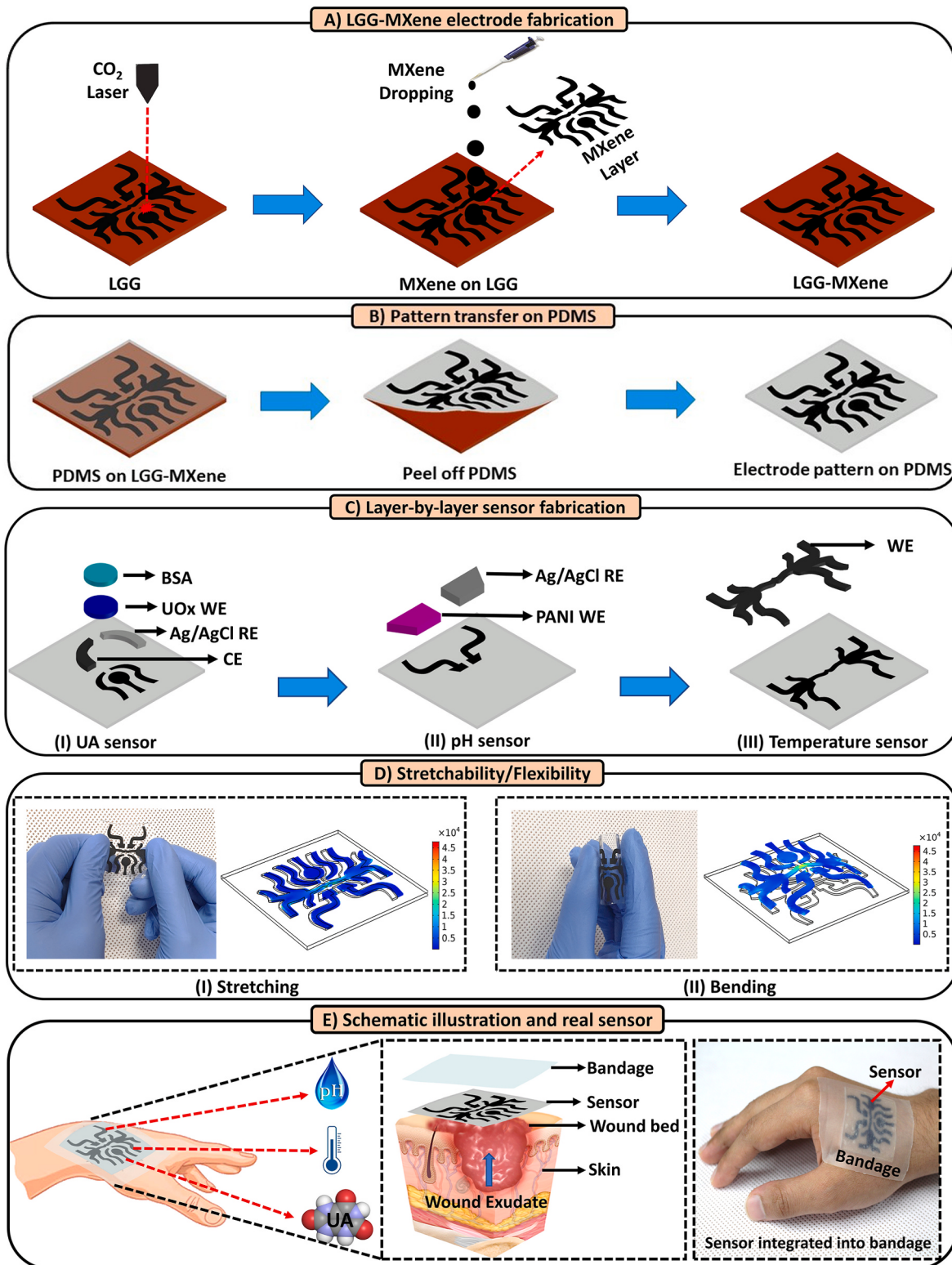
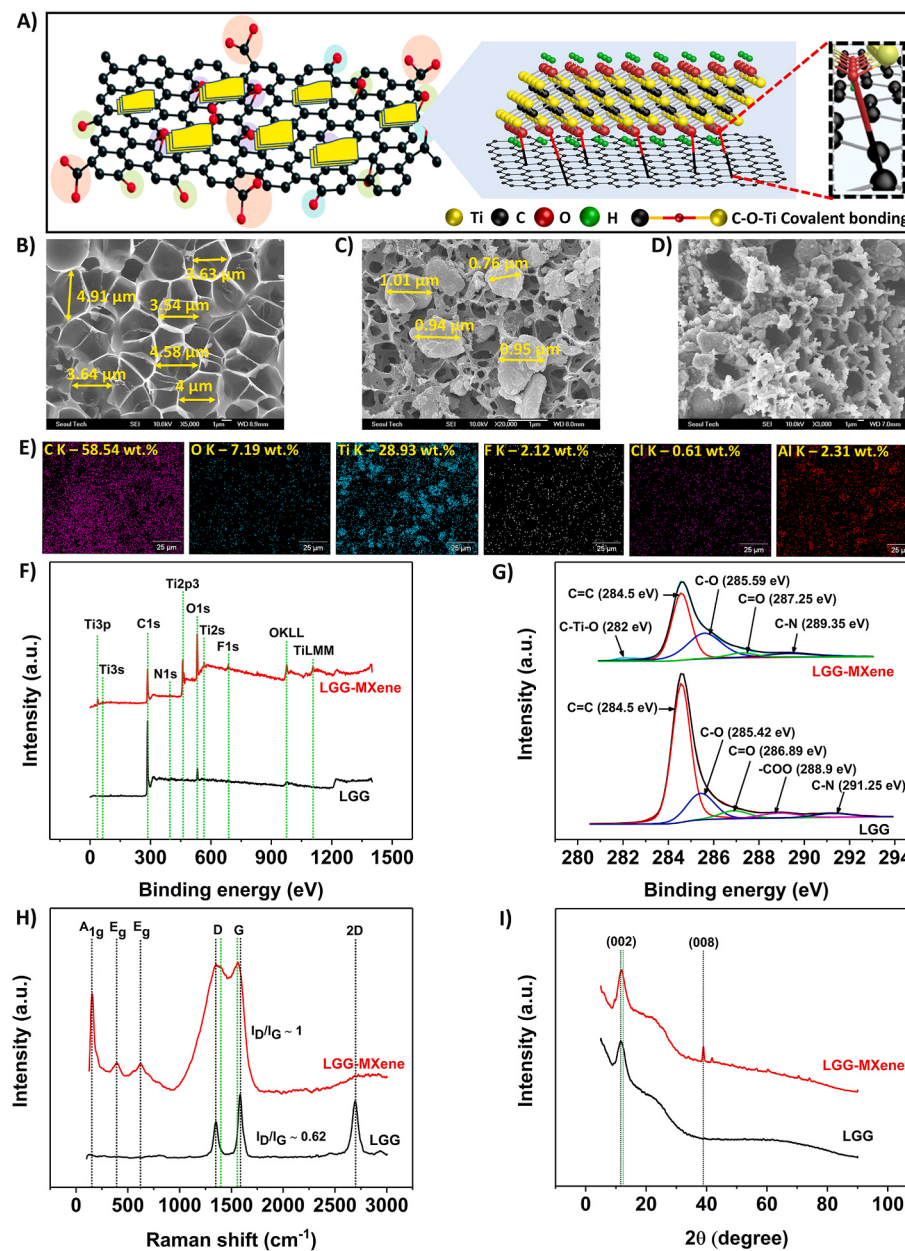


Fig. 1. Stepwise fabrication scheme of the proposed stretchable and flexible smart bandage with an integrated multifunctional sensor. A) LGG-MXene electrode fabrication. B) Transferring the pattern onto PDMS using the peel-off process. C) Layer-by-layer sensor fabrication (I) UA sensor, (II) pH sensor, and (III) temperature sensor. D) COMSOL simulation for stress distribution on electrode traces with a stress of 3 mm ((I) stretching and (II) bending). E) Schematic illustration and a photograph of the stretchable and flexible smart bandage embedded on an object's hand.

functionalization process (Fig. 1A and Fig. S3 (A-C)). It was then dried at room temperature for 5 min. The high solubility and evaporation rate of ethanol in air accelerated the drying process of the patterns without altering the base architecture. MXene nanosheets were likely dispersed into the desired patterns through the percolation process; they infiltrated the bottom surface of the LGG sheets via the porous network. Second, a vacuum-degassed PDMS solution (base: curing agent = 10:1) was carefully poured onto the LGG-MXene hybrid scaffold. After successful thermal curing at 85 °C for 1.5 h, the LGG-MXene/PDMS sheet was slowly peeled off from the PI film. (Fig. 1B).

The layer-by-layer fabrication procedure of the UA sensor is illustrated in Fig. 1C(I). The UA sensor consisted of three electrodes: WE (LGG-MXene/PDMS), CE (LGG-MXene/PDMS), and RE (Ag/AgCl). The WE was fabricated according to a previous study with some modifications (Kassal et al., 2015). First, 7 µL of uricase (UOx) was immobilized with the help of glutaraldehyde and then incubated for 5 h at 4 °C to ensure the proper binding of UOx with the surface functional groups of LGG-MXene through a hydrogen bond. Finally, 6 µL of BSA was drop-casted to eliminate the nonspecific binding molecules.



The potentiometric pH sensor was designed and fabricated according to previous literature (Zahed et al., 2020). Briefly, the fabricated pH sensor comprised two electrodes: RE and WE. Ag/AgCl and PANI/LGG-MXene served as the RE and WE, respectively, where PANI was deployed as a pH-sensitive membrane (Fig. 1C(II)). PANI was electropolymerized on the WE in a 0.1 M aniline/1 M HCl aqueous solution by CV techniques (potential range: -0.2 to 1 V, scan rate: 100 mV s⁻¹, segments: 60). During electropolymerization, the anodic and cathodic peak currents gradually increased with the increasing numbers of deposition segments, which ensured the successful deposition of PANI (Fig. S4).

The temperature sensor used a direct LGG-MXene/PDMS electrode (Fig. 1C(III)) as a thermistor with a unique layout covering the nearby area of the chronic wounds. For chronic wound temperature sensors, the material architecture and sensor mapping are important for capturing the desired information related to wound healing (Hattori et al., 2014).

The stretchability and flexibility of the electrode array under different mechanical deformations, such as stretching and bending, were exhibited and verified by COMSOL simulations, as shown in Fig. 1D. For

Fig. 2. A) Schematic model of LGG-MXene hybrid scaffold exhibiting the formation of C-O-Ti covalent crosslink. FESEM images of B) LGG/PDMS (average pore diameter of the LGG sheets is ~4 µm), C) LGG-MXene/PDMS (average width of the MXene nanosheets is ~0.90 µm), and D) PANI/LGG-MXene/PDMS. E) EDX elemental mapping of C, O, Ti, F, Cl, and Al for LGG-MXene. F) XPS survey spectra of LGG and LGG-MXene. G) High-resolution C1s spectra of LGG and LGG-MXene. H) Raman shift spectra of LGG and LGG-MXene. I) XRD patterns of LGG and LGG-MXene.

both cases (Fig. 1D(I) and (II)), COMSOL finite element analysis (FEA) was applied to measure the stress distributions on the electrode traces for a stress of 3 mm. Finally, the fully fabricated construct was embedded onto a transparent commercial medical tape to create a wearable platform suitable for chronic wound monitoring. Fig. 1E shows a schematic illustration and a real photograph of the stretchable and flexible smart bandage with integrated multifunctional sensors embedded on the object's hand for detecting various physiochemical wound markers.

3. Results and discussion

3.1. Functionalization of 3D LGG sheets using 2D MXene

The oxygen-containing hydrophilic surface functional groups of MXene nanosheets react with the carboxyl (-COOH) and hydroxyl groups (-OH) of the LGG sheets at room temperature to form a C–O–Ti covalently cross-linked LGG-MXene hybrid scaffold via nucleophilic substitution (Fig. 2A). Covalent crosslinking in C–O–Ti plays a significant role in building the hybrid scaffold, thereby boosting the linking of the LGG and MXene nanosheets and facilitating high electron mobility. The reaction mechanism for the realization of C–O–Ti covalent crosslink bonding between LGG and MXene is as follows:

3.2. Physical characterization of LGG-MXene electrodes

The FESEM analysis of the as-transferred bare LGG onto PDMS exhibited a well-patterned 3D microporous network (Fig. 2B). During MXene functionalization, the microporous structure of LGG flakes ($\sim 4 \mu\text{m}$ pore diameter, Fig. 2B) facilitated the infiltration of MXene nanosheets ($\sim 0.90 \mu\text{m}$ wide, Fig. 2C) through the porous network to the bottom side of the LGG sheets to form the 3D-2D hybrid scaffold, providing excellent surface conductivity after transfer onto PDMS. Fig. S3(A-C) illustrates the surface morphologies of the as-transferred LGG-MXene/PDMS for 1, 3, and 5 mg mL⁻¹ loading of MXene. In the cases of 1 and 3 mg mL⁻¹ loading (Figs. S3A and S3B), fewer MXene nanosheets penetrated the bottom side, whereas for the 5 mg mL⁻¹ loading (Fig. S3C), many active MXene nanosheets penetrated and covered the bottom surface, forming the 3D-2D hybrid scaffold. The final FESEM image of the as-transferred LGG-MXene/PDMS electrode for the 5 mg mL⁻¹ loading (optimized) of MXene is depicted in Fig. 2C. The pH-sensitive PANI membrane was electropolymerized onto the optimized electrode for the fabrication of the pH sensor. Fig. 2D shows the FESEM image, evidencing the growth of the grass-like PANI membrane onto the LGG-MXene/PDMS electrode. Furthermore, the FESEM-EDS elemental mapping of LGG-MXene (Fig. 2E) depicts the atomic weight distribution of C (58.54%), O (7.19%), Ti (28.93%), F (2.12%), Cl (0.61%), and Al (2.31%), thereby confirming the presence of MXene in LGG.

The chemical compositions of LGG and LGG-MXene were investigated by XPS analysis, as presented in Fig. 2F–G. The survey spectrum (Fig. 2F) of LGG exhibited the appearance of C, N, and O elements, whereas the LGG-MXene hybrid scaffold exhibited the appearance of Ti, C, N, O, and little F elements. The high-resolution C1s spectra (Fig. 2G) of bare LGG exhibited five peaks at different binding energies (BEs) of 284.5, 285.42, 286.89, 288.9, and 291.25 eV, which are associated with the chemical bonds of C=C, C–O, C=O, -COO, and C–N, respectively (Yoon et al., 2020). In contrast, the C1s spectra of LGG-MXene exhibited peaks at BEs of 284.5, 285.59, 287.25, 289.35 eV, which are associated with the bonds of C–Ti–O, C=C, C=O, and C–N, respectively (Ma et al., 2018). In the case of LGG-MXene, the peak intensity of the C–O bonds increased, which ensured the presence of MXene in the hybrid scaffold (Fan et al., 2018). In addition, a new peak was located at a BE of 282 eV, which is assigned to the C–O–Ti bonds, confirming the formation of a covalent bond between MXene and LGG during functionalization (Ma et al., 2018). Furthermore, the presence of high-resolution single C1s,

O1s, N1s, Ti2P, F1s, and core level Ti2P (Figs. S5A and S5B) spectra in LGG-MXene confirmed the successful functionalization process.

The chemical existence state of MXene nanosheets in the hybrid scaffold after functionalization was further analyzed via Raman spectroscopy, as presented in Fig. 2H. For bare LGG, three legible Raman peaks were observed at 1349 cm⁻¹ (D band represents the structural defects and disorder in the lattice), 1587 cm⁻¹ (G band represents the first-order phonon vibration due to C–C bond lattice stretching), and 2694 cm⁻¹ (2D band represents second-order phonon vibration due to C–C bond lattice stretching), suggesting the presence of graphenic materials (Ferrari et al., 2006). Moreover, the analyzed peak intensity ratio of the D-band and G-band for LGG was found to be ~ 0.62 (I_D/I_G), indicating an acceptable amount of defect in the LGG sheets (Vinayan et al., 2012). After MXene functionalization, three distinct modes were observed at 154 cm⁻¹ (corresponding to the A1g symmetry of the out-of-plane vibrations of Ti atoms), 392 cm⁻¹, and 626 cm⁻¹ (corresponding to the E_g in-plane group vibrations of Ti, C, and the surface terminal functional groups atoms), thereby confirming the existence of MXene nanosheets in the hybrid scaffold. Furthermore, the I_D/I_G ratio of the LGG-MXene increased to ~ 1 in comparison to that of ~ 0.62 for bare LGG sheets, which was possibly due to the reaction between MXene and LGG during functionalization (Zhou et al., 2020). In addition, the D-band and G-band peaks of LGG-MXene shifted from the D-band and G-band peaks of bare LGG sheets, demonstrating the successful formation of C–O–Ti covalent crosslinks between MXene and LGG (Zhou et al., 2020).

The comparison of the interlayer d-spacing changes in the bare LGG sheets with the LGG-MXene film was inspected by XRD analysis. Both films exhibited similar and excellent crystalline structures, as evident in Fig. 2I. The bare LGG exhibited a legible characteristic 2θ peak at $\sim 11.45^\circ$, corresponding to the (002) plane. When MXene nanosheets were loaded into the LGG sheets, the 2θ peak of LGG-MXene increased to $\sim 12.05^\circ$ owing to the increase in d-spacing, which facilitated the ion transfer rate (Fan et al., 2018). Moreover, the appearance of the (008) diffraction peak at $\sim 39.97^\circ$ further confirmed the presence of MXene in the hybrid scaffold during functionalization (Zhou et al., 2020).

3.3. Electrochemical studies of LGG-MXene electrodes and as-fabricated UA sensor

CV analysis was performed in a [PBS (pH 7.4) + 5.0 mM K₃/K₄] redox mediator to investigate the HET rate of the electrodes modified with different loading concentrations of MXene on LGG. Hence, the HET rate is a crucial factor for evaluating the performance of the electrode material. A fast HET rate indicates fast electron kinetics at the interface, leading to a highly conductive electrode material suitable for electrochemical applications (Rosli et al., 2020). The investigations in Fig. S3D show that the redox peak current increased gradually with the increasing loading concentration of MXene from 1 to 5 mg mL⁻¹. At a loading concentration of 5 mg mL⁻¹, the electrode exhibited the highest redox current; therefore, a fast HET rate was observed at the electrode interface owing to the presence of more active MXene nanosheets enforcing the synergistic effect. With further increasing the loading concentration of MXene to 7 mg mL⁻¹, the redox current showed insignificant change. This could be described by the excessive and ineffective restacking of MXene nanosheets on the electrode surface (J. Liu et al., 2019). Moreover, the irreversible stacking phenomenon caused by the excessive loading of MXene hinders the fast HET rate (Hu et al., 2016). Therefore, 5 mg mL⁻¹ of MXene loading leads to the best HET. Furthermore, the diffusion kinetics or control process of the redox mediator at the electrode interface was analyzed through CV (Fig. S6) to justify the fast HET rate.

The working principle of the fabricated UA sensor is schematically depicted in Fig. 3A. The layer-by-layer modification steps related to the fabrication of the UA sensor were investigated through CV and EIS analysis in a [PBS (pH 7.4) + 5.0 mM K₃/K₄] redox mediator, as shown

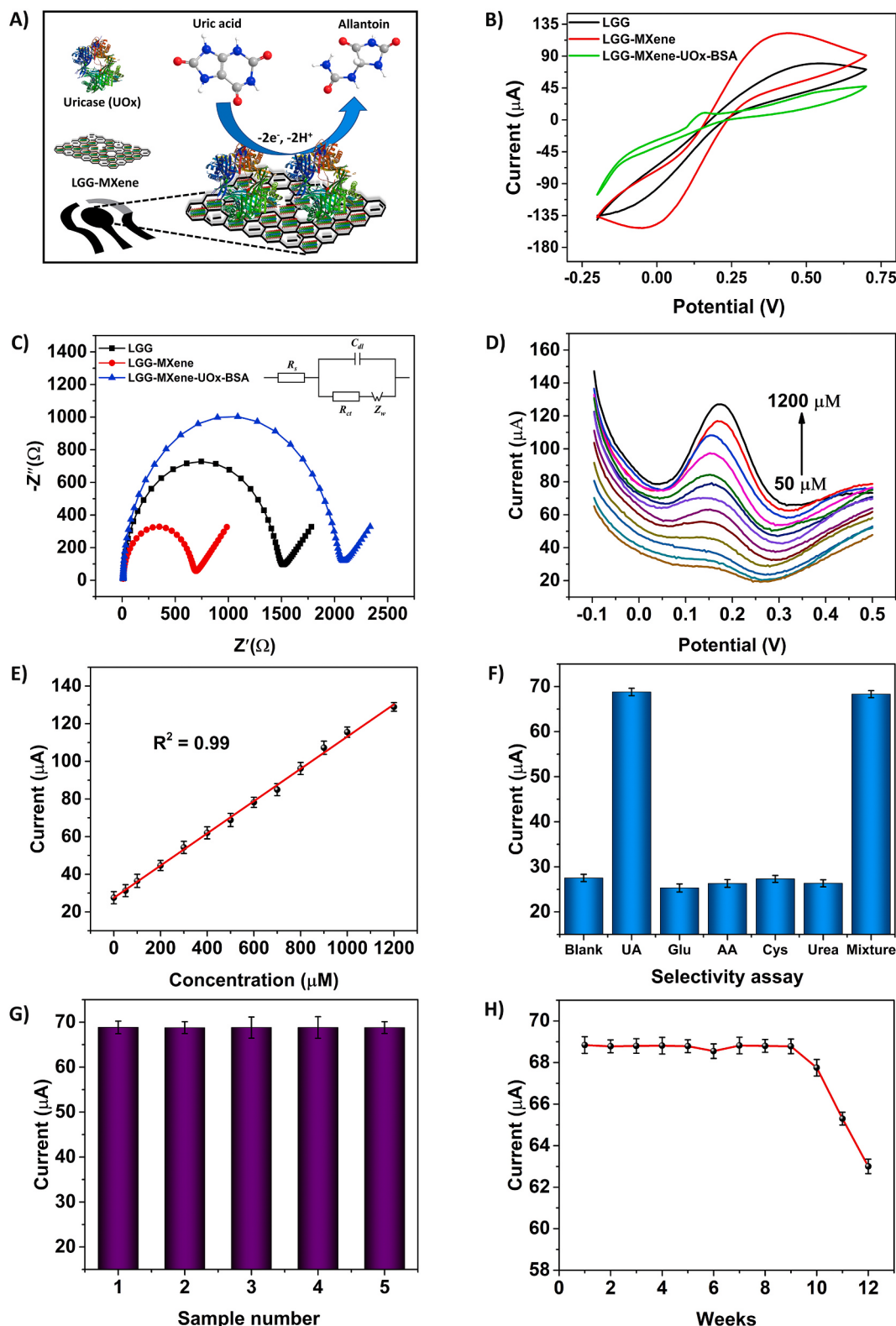
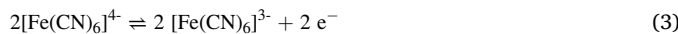
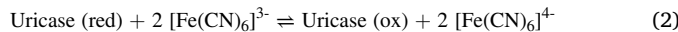
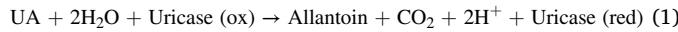


Fig. 3. A) Schematic illustrating the working mechanism of the UA sensor. B) CV performance comparison of bare LGG/PDMS, LGG-MXene/PDMS, and LGG-MXene-UOx-BSA/PDMS. C) EIS measurements of bare LGG/PDMS, LGG-MXene/PDMS, and LGG-MXene-UOx-BSA/PDMS (the inset indicates the Randles equivalent model). D) DPV response toward the oxidation of UA over an extended linear range of 50–1200 μ M. E) Calibration plot for the linear range. F) Selectivity measurement against various interferences using the DPV response. G) Reproducibility test using the DPV response. H) Stability test over 12 weeks.

in Fig. 3B–C. As shown in Fig. 3B, after functionalization (loading of 5 mg mL⁻¹ MXene), the LGG-MXene/PDMS electrode exhibited the highest redox current compared to the bare LGG/PDMS electrode. This reveals that the presence of MXene on LGG through the functionalization process enhances the HET rate at the electrode interface. In contrast, the application of the 3D-2D hybrid scaffold with highly conductive MXene nanosheets onto a rich porous network can evidently increase its effective surface area. However, when the UOx along with BSA was immobilized onto the electrode, the redox current significantly decreased because the electron transfer was obstructed by the enzyme and protein layers.

The interfacial interactions of the as-fabricated electrodes were explored by EIS measurements in a 5.0 mM K₃/K₄ redox mediator, as shown in Fig. 3C. The Randles electric circuit configuration (inset Fig. 3C) was modeled to simulate the experimental results, where C_{dL}, Z_w, R_{ct} and R_s correspond to the double-layer capacitance, Warburg element impedance, charge transfer resistance, and solution resistance, respectively. The exact diameter of the semicircle of the Nyquist plot characterizes the charge transfer resistance (R_{ct}). The bare LGG exhibited a large R_{ct} value of 1511 Ω owing to the poor conductivity of LGG sheets. With MXene functionalization, the interfacial R_{ct} value decreased significantly to 682 Ω, which was ascribed to the excellent conducting properties of the accordion-like MXene nanosheets. Again, the deposition of UOx along with BSA increased the R_{ct} value to 2061 Ω, which was attributed to the presence of the electron blocking layer.

Fig. 3D shows the DPV response of the UA sensor in the [PBS (pH 7.4) + 5.0 mM K₃/K₄] redox mediator toward the oxidation of UA over an extended linear range of 50–1200 μM. Under ideal conditions, when the background signal was stable, a successive increase in the DPV peak currents was observed at the electrode with the increasing injection of UA concentrations due to the catalytic oxidation of UA (Verma et al., 2019). The UA detection mechanism at the electrode interface via the K₃/K₄ redox mediator can be ascribed to the following chemical reactions (Equation (1)–(3)), where the oxidation of UA into allantoin is catalyzed by uricase, and thus, uricase is reduced.



The calibration plot (Fig. 3E) demonstrates a collinear relationship between the DPV peak currents and UA concentration ranging from 50–1200 μM with an excellent regression coefficient (R²) and sensitivity of 0.999 and 422.5 μA mM⁻¹ cm⁻², respectively. The LOD of 50 μM was determined by the standard formula, which is appreciably lower than the clinically acceptable level of UA concentration in wound exudates (Kassal et al., 2015). The extended linear range, ultralow LOD, and excellent sensitivity achieved by the as-fabricated UA sensor suggest its promising applicability in clinical applications in comparison to previously reported wound-based UA sensors (Table S1).

The selectivity of the UA sensor was investigated by comparing the DPV response for 500 μM UA against other electrochemically active interfering molecules present in wound exudates, such as glucose (Glu), ascorbic acid (AA), cysteine (Cys), urea, and cocktail mixture with ten times higher concentrations. The results in Fig. 3F justify the high selectivity and specificity of the developed sensor toward UA only.

The reproducibility of the UA sensor was assessed on five individual electrodes by measuring DPV currents of 500 μM UA individually under ideal conditions. The calculated relative standard deviation (RSD) from the plotted graphs in Fig. 3G was found to be 4.26%, which is less than 5%, thereby suggesting the satisfactory reproducibility features of the developed sensors.

The storage stability and batch to batch stability performance of the fabricated sensors were verified at stipulated time intervals again by measuring DPV currents of 500 μM UA (Figs. 3H and S7). Up to nine

weeks, over 96% of the initial DPV responses remained, thereby revealing the long-term self-lifetime of the UA sensor.

3.4. Electrochemical studies of as-fabricated pH sensor

The working principle of the as-fabricated potentiometric pH sensor (Fig. 4A) relates the reversible protonation/deprotonation of the PANI-deposited WE under an acid/base environment, where the open circuit potential (OCP) output resulting from charge accumulation could be calculated for the assessment of pH.

Fig. 4B shows the OCP vs. time profile of the fabricated pH sensor with variations in pH in different standard pH solutions in terms of decreasing and increasing the pH, ranging from 9 to 4 and back to 9 (wound exudate-relevant range). The sensor exhibited a linear Nernstian response with a high sensitivity and regression coefficient (R²) of -57.03 mV pH⁻¹ and 0.998, respectively, as plotted in Fig. 4C, which is better than the previously reported wound based pH sensors (Table S2).

The repeatability of the pH sensors was evaluated in three titrated cycles over a wide pH range of 9–4 under ideal conditions, as illustrated in Fig. 4D. After three successive repetitions, the pH sensor yielded an average sensitivity of -56.80 mV pH⁻¹, which is almost similar to its initial sensitivity, demonstrating the excellent repeatability of the developed sensor.

The selectivity of the fabricated pH sensor at different pH levels was investigated in the presence of other ionic compositions related to wounds, including UA, K⁺, Na⁺, Ca²⁺, NH₄⁺, and Glu, as depicted in Fig. 4E. The sensor showed insignificant response for other ions owing to the effective coating of the H⁺ sensitive PANI membrane on the WE.

The stability of the fabricated pH sensor was evaluated by immersing the sensors at the lowest and highest pH levels (4 and 9); the changes in the OCP values were observed over stipulated time intervals. As evident in Fig. 4F, the sensor showed a stable OCP response over a 23 h period with a drift of less than 10 mV, indicating the excellent stability of the sensor for wound assessing application (Mostafalu et al., 2018). Furthermore, the batch to batch stability performance of the pH sensors (5 batches) was examined by measuring the OCP values at pH = 8 (Fig. S8).

3.5. Characterization of as-fabricated temperature sensor

The working mechanism of the temperature sensor is illustrated in Fig. 5A. The LGG-MXene/PDMS electrode has an excellent thermoresistive effect, which was used for designing the temperature sensor. When temperature rises, its resistance increases, thereby demonstrating the positive temperature coefficient resistance (PTCR) behavior due to the thermal expansion of the polymeric PDMS electrode at an elevated temperature, which creates a crack between the hybrid scaffold and increases the phonon scattering in the sandwiched layers (Yang et al., 2015, 2020). The temperature sensor exhibited a fast, precise, and reliable response to the temperature variations over 25–50 °C with an excellent sensitivity and correlation coefficient (R²) of 0.09% °C⁻¹ and 0.999, respectively, as illustrated in Fig. 5B, which is comparable to the previously reported temperature sensors (Table S3). Fig. 5C shows the resistance vs. temperature plot, demonstrated the PTCR behavior of the fabricated sensor, where the resistance increased from 788 Ω at 25 °C to 805 Ω at 50 °C. A closer investigation of Fig. 5C indicates that resistance did not change linearly with the increasing temperature, which can be characterized by the following expression (Shahil and Balandin, 2012).

$$R = R_0 \exp \left(\frac{E_a}{2KT} \right) = R_0 \exp \left(\frac{B}{T} \right) \quad (4)$$

where R denotes the resistance at T, R₀ is the resistance at T = ∞, E_a is the activation energy, K is the Boltzmann constant, and B is the thermal index. Equation (4) can be modified as

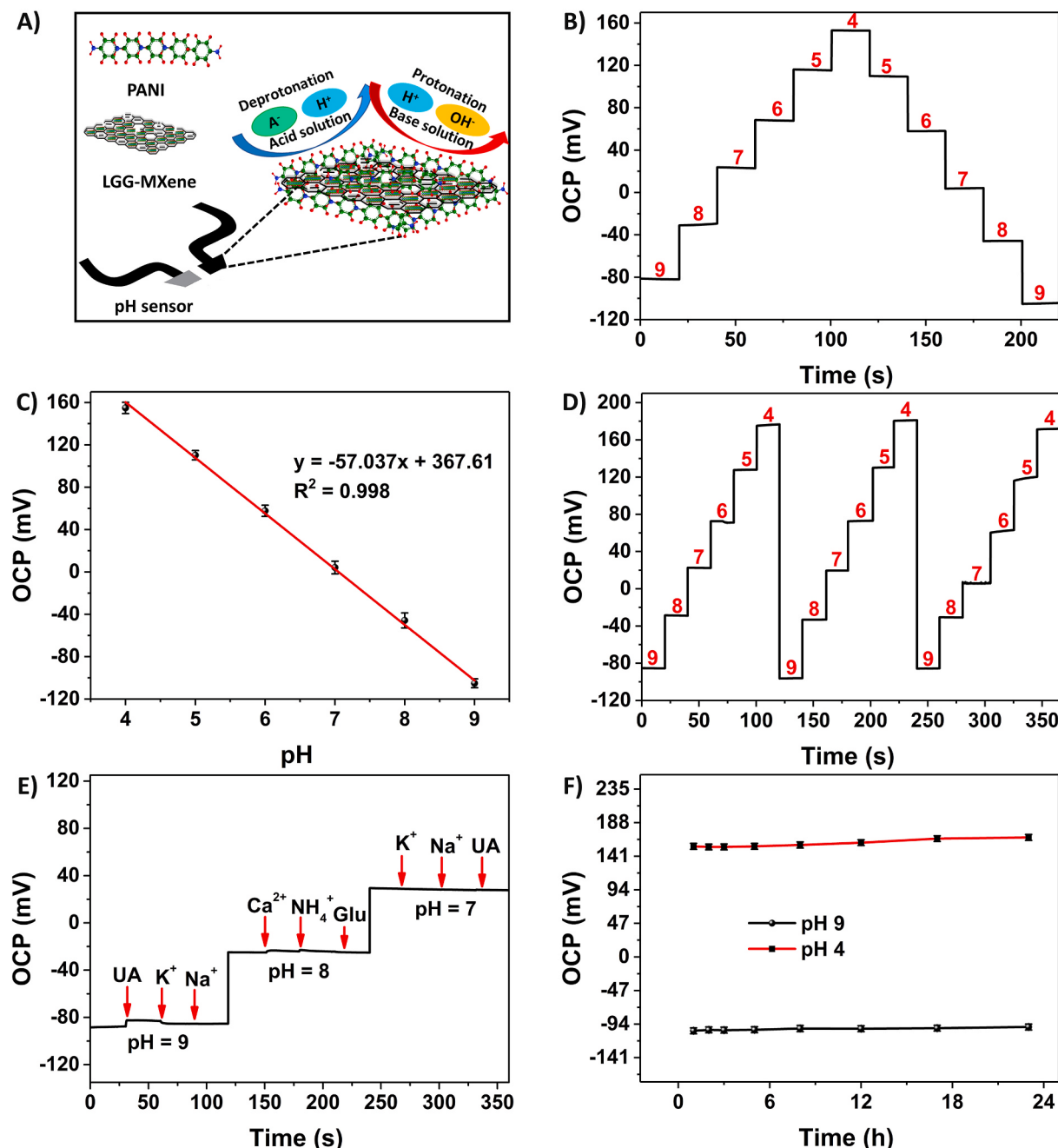


Fig. 4. A) Schematic illustrating the working mechanism of the pH sensor. B) OCP response of the pH sensor with decreasing and increasing pH ranging from 9 to 4 and back to 9. C) Calibration plot of OCP vs. pH. D) Repeatability test in three-titrated cycles. E) Selectivity test of the pH sensor at different wound relevant pH levels (9, 8, and 7) in the presence of other wound-related ionic compositions such as UA, K⁺, Na⁺, Ca²⁺, NH₄⁺, and Glu. The OCP output values due to the interfering substances were insignificant indicating the high selectivity of the pH sensor. F) OCP response at high and low pH levels over 24 h, demonstrating the stability performance.

$$\ln(R) = \ln(R_0) + \frac{E_a}{2KT} = \ln(R_0) + \frac{B}{T} \quad (5)$$

where ln(R) and 1/T profiles are expected to exhibit a linear relationship. Fig. 5D shows the linear fitting result for the calculated data (black circles). For practical applications, a linear relationship is very important because it simplifies the real-time measurement steps (Yan et al., 2015).

The dynamic temperature response of the sensor was also analyzed by applying incremental temperatures from 30 to 45 °C (physiological temperature range) with 15 s intervals at every step, as shown in Fig. 5E. The sensor also exhibited a fast and stable PTCR response to the step

temperature, thereby elucidating a potential candidate material for wound temperature monitoring (Yang et al., 2020). The batch to batch stability performance of the as-fabricated temperature sensors (5 batches) was investigated by measuring the sensitivity at different batches (Fig. S9).

3.6. In vitro analysis of real-time applications

To evaluate the analytical reliability of the fabricated UA sensor for practical applications, the standard addition method was deployed to quantify the real recoveries of different concentrations of spiked UA in artificial wound exudate samples (see experiment section for the

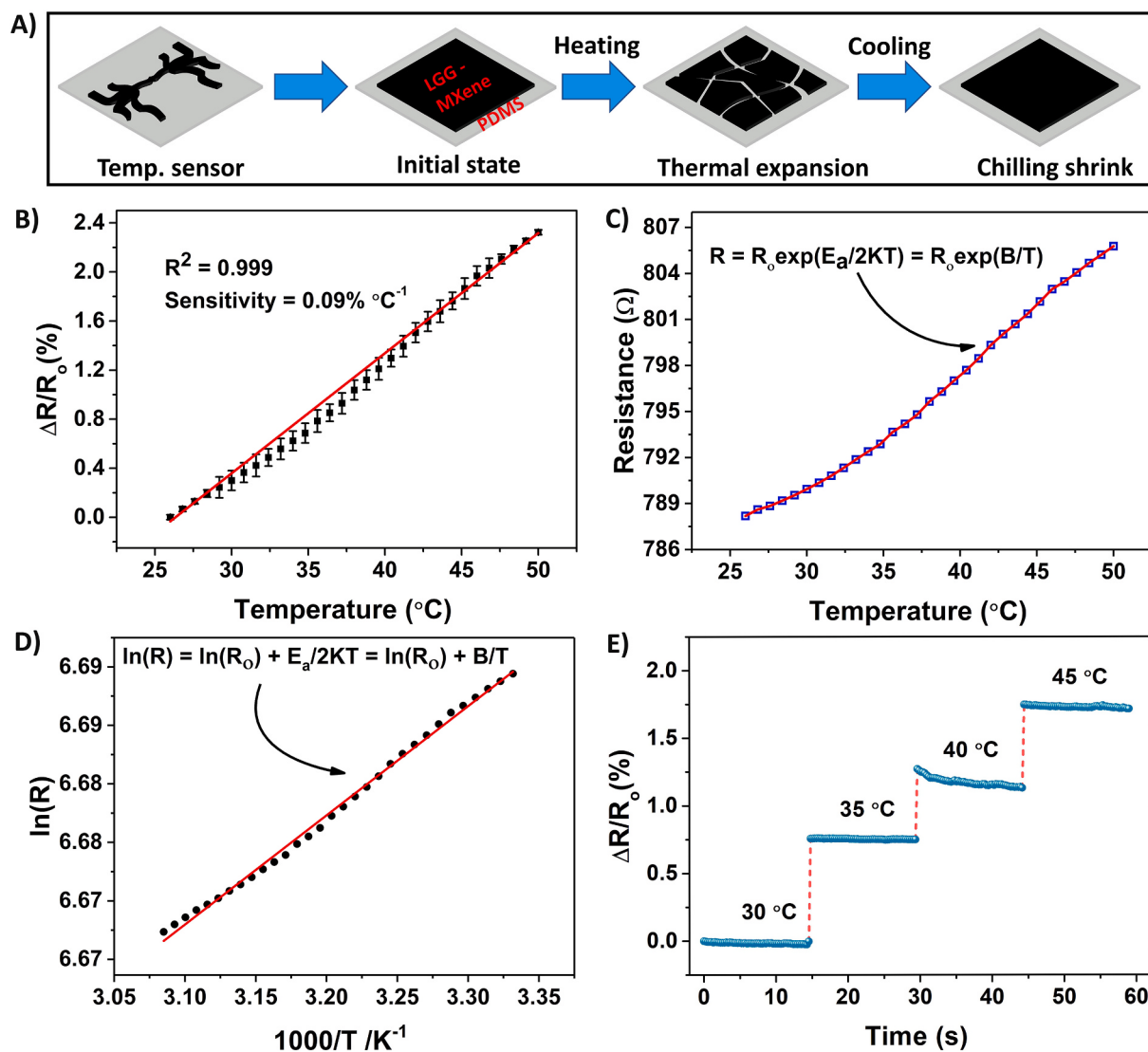


Fig. 5. A) Schematic illustrating the working mechanism of the temperature sensor. B) Relative resistance changes in the temperature sensor as a function of temperature indicating the PTCR behavior of the temperature sensor. C) Resistance variation with temperature exhibiting a nonlinear relationship. D) Dependence of $\ln(R)$ on $1000/T$ exhibiting a linear relationship. E) Dynamic response of the temperature sensor with incremental temperatures in the physiological range.

preparation procedure of artificial sample), as shown in Fig. 6A. For each spiked UA concentration, the recovery rate and RSD were calculated to be (102.5–101.3)% and (1.15–1.02)%, respectively, suggesting the practicability of the UA sensor for the real-time monitoring of UA concentrations in wound exudates.

To date, there are no latest standard methods for the in vitro measurements of the function of pH sensors for wound applications. Thus, the reliability, feasibility, and accuracy of the developed pH sensor was evaluated by measuring the artificial wound fluids with different pH values and comparing the results with those achieved using a commercial pH meter, as illustrated in Fig. 6B and C. The pH values measured from the pH sensor at different pH levels (9–4, wound exudate-relevant range) were nearly comparable to those obtained from the commercial pH meter.

For real-time monitoring, the dynamic response of the temperature sensor upon removal from and contact with the human skin was analyzed and is demonstrated in Fig. 6D and E. The parameters were measured through the resistance variations of the sensor caused by its cyclic removal and contact with the human skin. Once the sensor was isolated from the skin, the resistance dropped suddenly and then saturated within a few seconds. In contrast, when the sensor touched the

skin, the resistance increased exponentially to the initial level of contact resistance.

4. Conclusion

In summary, we successfully demonstrated a facile method to functionalize 3D porous LGG sheets using MXene nanosheets through C–O–Ti covalent crosslinks to obtain LGG-MXene hybrid scaffold exhibited high conductivity and improved electrochemistry. After carefully transferring the obtained LGG-MXene hybrid scaffold onto PDMS, we engineered a smart, stretchable, and flexible multifunctional sensors-integrated wound bandage capable of detecting UA, pH, and temperature at the wound site. The flexible smart bandage showed excellent clinical linearity, sensitivity, repeatability, and stability for detecting UA, pH, and temperature both in analytical and real samples. Furthermore, the analytical and physiological detection limit exhibited by our sensor covers the normal physicochemical levels of UA, pH, and temperature in a healthy human, suggesting its promising potential in clinical applications. This flexible LGG-MXene hybrid scaffold can be a promising candidate for various wearable functional electronics including biosensors and energy storage. In the foreseeable future, we

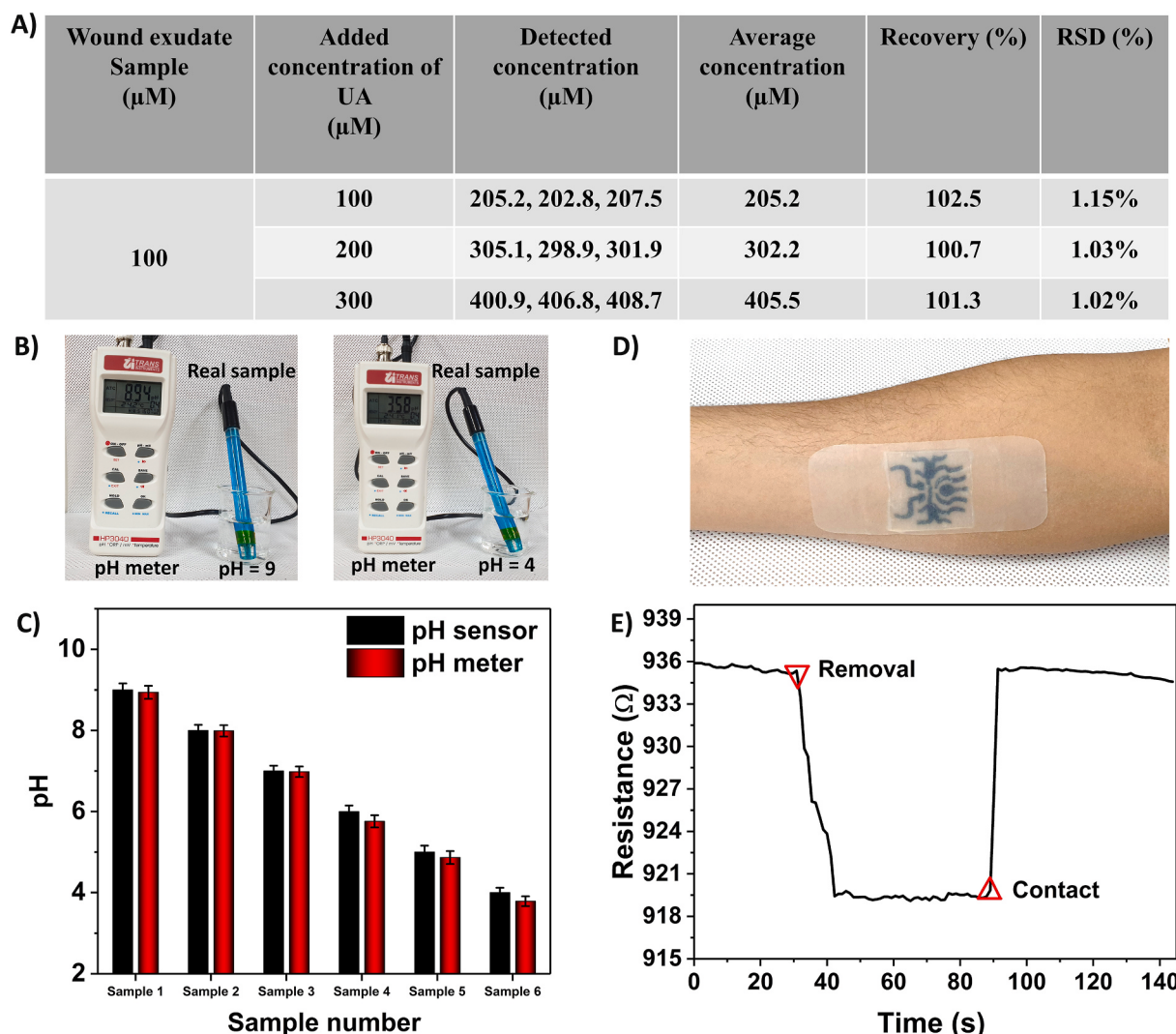


Fig. 6. A) Summary of the recovery rate of UA in artificial wound exudate. B) Optical images showing the commercial pH meter to detect pH from artificial wound fluids. C) Comparison plot demonstrating the performance of the developed pH sensor and commercial pH meter. D) Temperature sensor embedded on an object's skin. E) Dynamic response of the temperature sensor upon removal from contact with the skin.

plan to perform *in vivo* animal tests and integrate the sensor with a custom-designed flexible printed circuit, including a near-field communication module, to implement a real-time miniaturized advanced wound care management system.

CRediT Author Statement

Md. Sharifuzzaman: Conceptualization, Formal analysis, Writing – original draft, Validation. **Ashok Chhetry:** Investigation, Experimental analysis, & Editing. **Md. Abu Zahed:** Visualization, Writing – original draft, & Editing. **Sang Hyuk Yoon:** Methodology. **Chan I Park:** Methodology. **Shipeng Zhang:** Methodology. **Sharat Chandra Barman:** Writing – review & editing. **Sudeep Sharma:** Review & editing. **Hyo Sang Yoon:** Formal analysis, Methodology. **Jae Yeong Park:** Funding acquisition, Supervision.

Declaration of competing interest

The authors declare that they have no known competing financial interests or personal relationships that could have appeared to influence the work reported in this paper.

Acknowledgments

This work was supported by the Technology Innovation Program (200000773, Development of nanomultisensors based on wearable patch for nonhaematological monitoring of metabolic syndrome) funded by the Ministry of Trade, Industry & Energy (MI, Korea) and by the Bio & Medical Technology Development Program of the NRF grant funded by the Korean government (MSIT) (NRF-2017M3A9F1031270). Furthermore, the authors are grateful to the members of the ASER (Advanced Sensor and Energy Research Laboratory) group for their technical support and discussion.

Appendix A. Supplementary data

Supplementary data to this article can be found online at <https://doi.org/10.1016/j.bios.2020.112637>.

References

- Alhabeb, M., Maleski, K., Anasori, B., Lelyukh, P., Clark, L., Sin, S., Gogotsi, Y., 2017. Guidelines for synthesis and processing of two-dimensional titanium carbide (Ti 3 C 2 T x MXene). *Chem. Mater.* 29, 7633–7644. <https://doi.org/10.1021/acs.chemmater.7b02847>.

- Barman, S.C., Zahed, M.A., Sharifuzzaman, M., Ko, S.G., Yoon, H., Nah, J.S., Xuan, X., Park, J.Y., 2020. A polyallylamine anchored amine-rich laser-ablated graphene platform for facile and highly selective electrochemical IgG biomarker detection. *Adv. Funct. Mater.* 30, 1907297. <https://doi.org/10.1002/adfm.201907297>.
- Dabiri, G., Damstetter, E., Phillips, T., 2016. Choosing a wound dressing based on common wound characteristics. *Adv. Wound Care*. <https://doi.org/10.1089/wound.2014.0586>.
- Dargaville, T.R., Farrugia, B.L., Broadbent, J.A., Pace, S., Upton, Z., Voelcker, N.H., 2013. Sensors and imaging for wound healing: a review. *Biosens. Bioelectron.* <https://doi.org/10.1016/j.bios.2012.09.029>.
- Derakhshandeh, H., Kashaf, S.S., Aghabaglu, F., Ghanavati, I.O., Tamayol, A., 2018. Smart bandages: the future of wound care. *Trends Biotechnol.* <https://doi.org/10.1016/j.tibtech.2018.07.007>.
- Fan, Z., Wang, Y., Xie, Z., Wang, D., Yuan, Y., Kang, H., Su, B., Cheng, Z., Liu, Y., 2018. Modified MXene/holey graphene films for advanced supercapacitor electrodes with superior energy storage. *Adv. Sci.* 5, 1800750. <https://doi.org/10.1002/advs.201800750>.
- Ferrari, A.C., Meyer, J.C., Scardaci, V., Casiraghi, C., Lazzeri, M., Mauri, F., Piscanec, S., Jiang, D., Novoselov, K.S., Roth, S., Geim, A.K., 2006. Raman spectrum of graphene and graphene layers. *Phys. Rev. Lett.* <https://doi.org/10.1103/PhysRevLett.97.187401>.
- Ghidiu, M., Lukatskaya, M.R., Zhao, M.-Q., Gogotsi, Y., Barsoum, M.W., 2014. Conductive two-dimensional titanium carbide 'clay' with high volumetric capacitance. *Nature* 516, 78–81. <https://doi.org/10.1038/nature13970>.
- Gu, H., Xing, Y., Xiong, P., Tang, H., Li, C., Chen, S., Zeng, R., Han, K., Shi, G., 2019. Three-dimensional porous Ti3C2Tx MXene-graphene hybrid films for glucose biosensing. *ACS Appl. Nano Mater.* <https://doi.org/10.1021/acsnano.9b01465>.
- Hattori, Y., Falgout, L., Lee, W., Jung, S.Y., Poon, E., Lee, J.W., Na, I., Geisler, A., Sadhwani, D., Zhang, Y., Su, Y., Wang, X., Liu, Z., Xia, J., Cheng, H., Webb, R.C., Bonifas, A.P., Won, P., Jeong, J.W., Jang, K.I., Song, Y.M., Nardone, B., Nodzenski, M., Fan, J.A., Huang, Y., West, D.P., Paller, A.S., Alam, M., Yeo, W.H., Rogers, J.A., 2014. Multifunctional skin-like electronics for quantitative, clinical monitoring of cutaneous wound healing. *Adv. Healthc. Mater.* <https://doi.org/10.1002/adhm.201400073>.
- Hope, M.A., Forse, A.C., Griffith, K.J., Lukatskaya, M.R., Ghidiu, M., Gogotsi, Y., Grey, C.P., 2016. NMR reveals the surface functionalisation of Ti3C2 MXene. *Phys. Chem. Chem. Phys.* 18, 5099–5102. <https://doi.org/10.1039/C6CP00330C>.
- Hu, T., Hu, M., Li, Z., Zhang, H., Zhang, C., Wang, J., Wang, X., 2016. Interlayer coupling in two-dimensional titanium carbide MXenes. *Phys. Chem. Chem. Phys.* <https://doi.org/10.1039/c6cp01699e>.
- Huang, R., Chen, S., Yu, J., Jiang, X., 2019. Self-assembled Ti3C2/MWCNTs nanocomposites modified glassy carbon electrode for electrochemical simultaneous detection of hydroquinone and catechol. *Ecotoxicol. Environ. Saf.* 184, 109619. <https://doi.org/10.1016/j.ecoenv.2019.109619>.
- Hui, X., Xuan, X., Kim, J., Park, J.Y., 2019. A highly flexible and selective dopamine sensor based on Pt-Au nanoparticle-modified laser-induced graphene. *Electrochim. Acta* 328, 135066. <https://doi.org/10.1016/j.electacta.2019.135066>.
- Jiang, Q., Wu, C., Wang, Z., Wang, A.C., He, J.-H., Wang, Z.L., Alshareef, H.N., 2018. MXene electrochemical microsupercapacitor integrated with triboelectric nanogenerator as a wearable self-charging power unit. *Nano Energy* 45, 266–272. <https://doi.org/10.1016/j.nanoen.2018.01.004>.
- Kassal, P., Kim, J., Kumar, R., de Araujo, W.R., Steinberg, I.M., Steinberg, M.D., Wang, J., 2015. Smart bandage with wireless connectivity for uric acid biosensing as an indicator of wound status. *Electrochim. Commun.* 56, 6–10. <https://doi.org/10.1016/j.elecom.2015.03.018>.
- Kim, H., Wang, Z., Alshareef, H.N., 2019. MXetronics: electronic and photonic applications of MXenes. *Nano Energy* 60, 179–197. <https://doi.org/10.1016/j.nanoen.2019.03.020>.
- Kobylko, M., Kociak, M., Sato, Y., Urita, K., Bonnot, A.M., Kasumov, A., Kasumov, Y., Suenaga, K., Colliex, C., 2014. Ballistic- and quantum-conductor carbon nanotubes: a reference experiment put to the test. *Phys. Rev. B* 90, 195431. <https://doi.org/10.1103/PhysRevB.90.195431>.
- Kurz, A., Sessler, D.I., Lenhardt, R., 1996. Perioperative normothermia to reduce the incidence of surgical-wound infection and shorten hospitalization. *N. Engl. J. Med.* <https://doi.org/10.1056/NEJM199605093341901>.
- Liu, J., Jiang, X., Zhang, R., Zhang, Y., Wu, L., Lu, W., Li, J., Li, Y., Zhang, H., 2019. MXene-enabled electrochemical microfluidic biosensor: applications toward multicomponent continuous monitoring in whole blood. *Adv. Funct. Mater.* 29, 1807326. <https://doi.org/10.1002/adfm.201807326>.
- Liu, L., Wei, Y., Jiao, S., Zhu, S., Liu, X., 2019. A novel label-free strategy for the ultrasensitive miRNA-182 detection based on MoS₂/Ti3C2 nanohybrids. *Biosens. Bioelectron.* 137, 45–51. <https://doi.org/10.1016/j.bios.2019.04.059>.
- Ma, Z., Zhou, X., Deng, W., Lei, D., Liu, Z., 2018. 3D porous MXene (Ti 3 C 2)/reduced graphene oxide hybrid films for advanced lithium storage. *ACS Appl. Mater. Interfaces* 10, 3634–3643. <https://doi.org/10.1021/acsm.7b17386>.
- Mostafalu, P., Tamayol, A., Rahimi, R., Ochoa, M., Khalipour, A., Kiaee, G., Yazdi, I.K., Bagherifard, S., Dokmeci, M.R., Ziaie, B., Sonkusale, S.R., Khademhosseini, A., 2018. Smart bandage for monitoring and treatment of chronic wounds. *Small* 14, 1703509. <https://doi.org/10.1002/smll.201703509>.
- Nguyen, D.D., Tai, N.H., Chen, S.Y., Chueh, Y.L., 2012. Controlled growth of carbon nanotube-graphene hybrid materials for flexible and transparent conductors and electron field emitters. *Nanoscale*. <https://doi.org/10.1039/c1nr11328c>.
- Pal, A., Goswami, D., Cuellar, H.E., Castro, B., Kuang, S., Martinez, R.V., 2018. Early detection and monitoring of chronic wounds using low-cost, omniphobic paper-based smart bandages. *Biosens. Bioelectron.* 117, 696–705. <https://doi.org/10.1016/j.bios.2018.06.060>.
- Pang, Q., Lou, D., Li, S., Wang, G., Qiao, B., Dong, S., Ma, L., Gao, C., Wu, Z., 2020. Smart flexible electronics-integrated wound dressing for real-time monitoring and on-demand treatment of infected wounds. *Adv. Sci.* 7, 1902673. <https://doi.org/10.1002/advs.201902673>.
- Park, S., Vosguerichian, M., Bao, Z., 2013. A review of fabrication and applications of carbon nanotube film-based flexible electronics. *Nanoscale* 5, 1727. <https://doi.org/10.1039/c3nr33560g>.
- Percival, S.L., McCarty, S., Hunt, J.A., Woods, E.J., 2014. The effects of pH on wound healing, biofilms, and antimicrobial efficacy. In: *Wound Repair Regen.* <https://doi.org/10.1111/wrr.12125>.
- Phair, J., Joshi, M., Benson, J., McDonald, D., Davis, J., 2014. Laser patterned carbon-polyethylene mesh electrodes for wound diagnostics. *Mater. Chem. Phys.* <https://doi.org/10.1016/j.matchemphys.2013.10.035>.
- Posnett, J., 2008. *The Burden of Chronic Wounds in the uK Venous Leg Ulcers. NT.*
- Rahimi, R., Ochoa, M., Ziae, B., 2016. Direct laser writing of porous-carbon/silver nanocomposite for flexible electronics. *ACS Appl. Mater. Interfaces* 8, 16907–16913. <https://doi.org/10.1021/acsm.6b00295>.
- Rosli, N.F., Rohaizad, N., Sturala, J., Fisher, A.C., Webster, R.D., Pumera, M., 2020. Siloxene, germanane, and methylgermanane: functionalized 2D materials of group 14 for electrochemical applications. *Adv. Funct. Mater.* <https://doi.org/10.1002/adfm.201910186>.
- Salvo, P., Dini, V., Kirchhain, A., Janowska, A., Oranges, T., Chiricozzi, A., Lomonaco, T., Di Francesco, F., Romanelli, M., 2017. Sensors and biosensors for C-reactive protein, temperature and pH, and their applications for monitoring wound healing: a review. *Sensors (Switzerland)*. <https://doi.org/10.3390/s17122952>.
- Schreml, S., Meier, R.J., Kirschbaum, M., Kong, S.C., Gehmert, S., Felthaus, O., Küchler, S., Sharpe, J.R., Wöltje, K., Weiß, K.T., Albert, M., Seidl, U., Schröder, J., Morszeck, C., Prantl, L., Duschl, C., Pedersen, S.F., Gosau, M., Berneburg, M., Wolfbeis, O.S., Landthaler, M., Babila, P., 2014. Luminescent dual sensors reveal extracellular pH-gradients and hypoxia on chronic wounds that disrupt epidermal repair. *Theranostics*. <https://doi.org/10.7150/thno.9052>.
- Seh, Z.W., Fredrickson, K.D., Anasori, B., Kibsgaard, J., Strickler, A.L., Lukatskaya, M.R., Gogotsi, Y., Jaramillo, T.F., Vojvodic, A., 2016. Two-dimensional molybdenum carbide (MXene) as an efficient electrocatalyst for hydrogen evolution. *ACS Energy Lett.* 1, 589–594. <https://doi.org/10.1021/acsenergylett.6b00247>.
- Sen, C.K., Gordillo, G.M., Roy, S., Kirsner, R., Lambert, L., Hunt, T.K., Gottrup, F., Gurtner, G.C., Longaker, M.T., 2009. Human skin wounds: a major and snowballing threat to public health and the economy: perspective article. In: *Wound Repair Regen.* <https://doi.org/10.1111/j.1524-475X.2009.00543.x>.
- Shahil, K.M.F., Balandin, A.A., 2012. Thermal properties of graphene and multilayer graphene: applications in thermal interface materials. *Solid State Commun.* <https://doi.org/10.1016/j.ssc.2012.04.034>.
- Sharp, D., Davis, J., 2008. Integrated urate sensors for detecting wound infection. *Electrochim. Commun.* 10, 709–713. <https://doi.org/10.1016/j.elecom.2008.02.025>.
- Song, W., Zhu, J., Gan, B., Zhao, S., Wang, H., Li, C., Wang, J., 2018. Flexible, stretchable, and transparent planar microsupercapacitors based on 3D porous laser-induced graphene. *Small* 14, 1–7. <https://doi.org/10.1002/smll.201702249>.
- Sun, B., McCay, R.N., Goswami, S., Xu, Y., Zhang, C., Ling, Y., Lin, J., Yan, Z., 2018. Gas-permeable, multifunctional on-skin electronics based on laser-induced porous graphene and sugar-templated elastomer sponges. *Adv. Mater.* 30, 1804327. <https://doi.org/10.1002/adma.201804327>.
- Tittle, C.M., Yilmaz, D., Pope, M.A., Backhouse, C.J., 2018. Robust superhydrophobic laser-induced graphene for desalination applications. *Adv. Mater. Technol.* 3, 1700207. <https://doi.org/10.1002/admt.201700207>.
- Verma, S., Choudhary, J., Singh, K.P., Chandra, P., Singh, S.P., 2019. Uricase grafted nanocombing matrix based electrochemical biosensor for ultrafast uric acid detection in human serum samples. *Int. J. Biol. Macromol.* <https://doi.org/10.1016/j.jbiomac.2019.02.121>.
- Vinayan, B.P., Nagar, R., Raman, V., Rajalakshmi, N., Dhathathreyan, K.S., Ramaprabhu, S., 2012. Synthesis of graphene-multiwalled carbon nanotubes hybrid nanostructure by strengthened electrostatic interaction and its lithium ion battery application. *J. Mater. Chem.* <https://doi.org/10.1039/c2jm16294f>.
- Wu, L., Lu, X., Dhanjai, Wu, Z.-S., Dong, Y., Wang, X., Zheng, S., Chen, J., 2018. 2D transition metal carbide MXene as a robust biosensing platform for enzyme immobilization and ultrasensitive detection of phenol. *Biosens. Bioelectron.* 107, 69–75. <https://doi.org/10.1016/j.bios.2018.02.021>.
- Xuan, X., Kim, J.Y., Hui, X., Das, P.S., Yoon, H.S., Park, J.-Y., 2018. A highly stretchable and conductive 3D porous graphene metal nanocomposite based electrochemical-physiological hybrid biosensor. *Biosens. Bioelectron.* 120, 160–167. <https://doi.org/10.1016/j.bios.2018.07.071>.
- Yan, C., Wang, J., Lee, P.S., 2015. Stretchable graphene thermistor with tunable thermal index. *ACS Nano.* <https://doi.org/10.1021/nn507441c>.
- Yang, J., Wei, D., Tang, L., Song, X., Luo, W., Chu, J., Gao, T., Shi, H., Du, C., 2015. Wearable temperature sensor based on graphene nanowalls. *RSC Adv.* <https://doi.org/10.1039/c5ra00871a>.
- Yang, Y., Song, Y., Bo, X., Min, J., Pak, O.S., Zhu, L., Wang, M., Tu, J., Kogan, A., Zhang, H., Hsiai, T.K., Li, Z., Gao, W., 2020. A laser-engraved wearable sensor for sensitive detection of uric acid and tyrosine in sweat. *Nat. Biotechnol.* 38, 217–224. <https://doi.org/10.1038/s41587-019-0321-x>.
- Yoon, H., Nah, J., Kim, H., Ko, S., Sharifuzzaman, M., Barman, S.C., Xuan, X., Kim, J., Park, J.Y., 2020. A chemically modified laser-induced porous graphene based flexible and ultrasensitive electrochemical biosensor for sweat glucose detection. *Sensor. Actuator. B Chem.* <https://doi.org/10.1016/j.snb.2020.127866>.
- Zahed, M.A., Barman, S.C., Das, P.S., Sharifuzzaman, M., Yoon, H.S., Yoon, S.H., Park, J.Y., 2020. Highly flexible and conductive poly (3, 4-ethylene dioxythiophene)-poly

(styrene sulfonate) anchored 3-dimensional porous graphene network-based electrochemical biosensor for glucose and pH detection in human perspiration. *Biosens. Bioelectron.* 160, 112220. <https://doi.org/10.1016/j.bios.2020.112220>.

Zhang, B., Li, W., Yang, Y., Chen, C., Li, C.-F., Saganuma, K., 2019. Fully embedded CuNWs/PDMS conductor with high oxidation resistance and high conductivity for stretchable electronics. *J. Mater. Sci.* 54, 6381–6392. <https://doi.org/10.1007/s10853-019-03333-x>.

Zhao, L., Dong, B., Li, S., Zhou, L., Lai, L., Wang, Z., Zhao, S., Han, M., Gao, K., Lu, M., Xie, X., Chen, B., Liu, Z., Wang, X., Zhang, Hao, Li, H., Liu, J., Zhang, Hua, Huang, X., Huang, W., 2017. Interdiffusion reaction-assisted hybridization of two-dimensional metal-organic frameworks and Ti₃C₂T_x nanosheets for electrocatalytic oxygen evolution. *ACS Nano* 11, 5800–5807. <https://doi.org/10.1021/acsnano.7b01409>.

Zhou, T., Wu, C., Wang, Y., Tomsia, A.P., Li, M., Saiz, E., Fang, S., Baughman, R.H., Jiang, L., Cheng, Q., 2020. Super-tough MXene-functionalized graphene sheets. *Nat. Commun.* 11, 2077. <https://doi.org/10.1038/s41467-020-15991-6>.